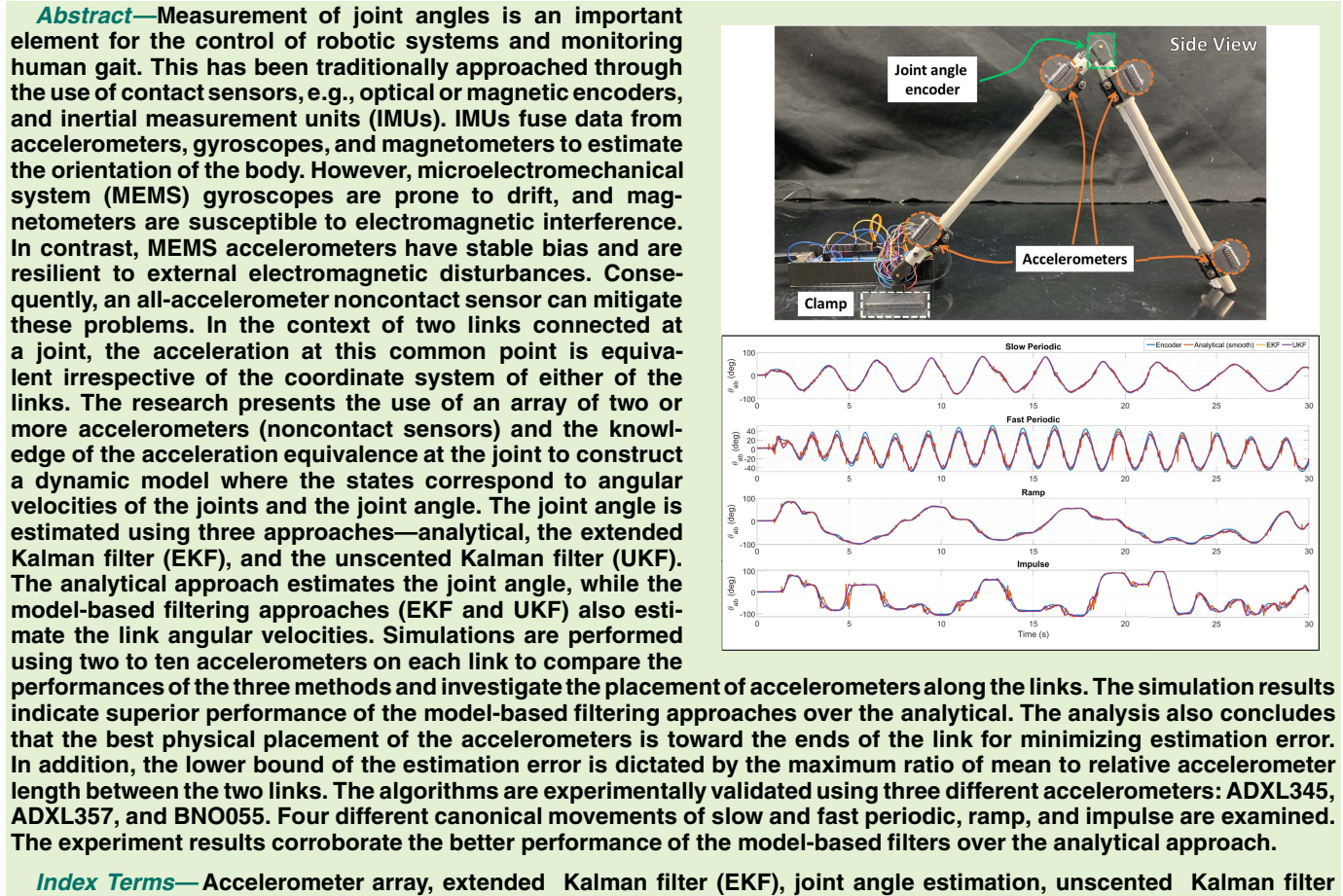


Joint Angle Estimation Using Accelerometer Arrays and Model-Based Filtering

Cole Woods^{ID}, Student Member, IEEE, and Vishesh Vikas^{ID}, Member, IEEE



Index Terms—Accelerometer array, extended Kalman filter (EKF), joint angle estimation, unscented Kalman filter (UKF).

I. INTRODUCTION

MASUREMENT and estimation of joint angles have been of interest to researchers in the domains of biomechanics, rehabilitation, wearables, robotics, and manufacturing [1], [2], [3], [4], [5], [6], [7], [8], [9], [10], [11]. For example, wearable devices for rehabilitation track a patient's

Manuscript received 15 July 2022; accepted 4 August 2022. Date of publication 25 August 2022; date of current version 14 October 2022. This work was supported by the National Science Foundation under Grant 1832993. The associate editor coordinating the review of this article and approving it for publication was Prof. Chang-Hee Won. (*Corresponding author: Vishesh Vikas*.)

The authors are with the Agile Robotics Lab (ARL), University of Alabama, Tuscaloosa, AL 35487 USA (e-mail: cswoods@crimson.ua.edu; vvikas@ua.edu).

Digital Object Identifier 10.1109/JSEN.2022.3200251

range of motion of desired joints. Given the nature of applications, the term joint angle refers to the angle between two links joined by a one degree-of-freedom revolute (or hinge) joint, e.g., knee and manipulator links.

The joint angles can be measured and estimated using contact (e.g., encoders) or noncontact sensors (e.g., accelerometers and gyroscopes). Contact sensors are directly placed at the joint and provide high-accuracy measurement. However, for a lot of applications, it is difficult to place an encoder without disturbing the integrity of the joint. For example, when dealing with the integration of encoders in wearable systems, they can be uncomfortable and burdensome. Recently, there has been research into soft wearable sensors [12]; however, they potentially interfere with the dynamics of the system.

In contrast, noncontact sensors are placed on the links and

away from the joint, providing design flexibility and wearability comfort without interfering with the system dynamics. Noncontact sensors comprise gyroscopes, accelerometers, magnetometers and their combination, and inertial measurement units (IMUs). Gyroscopes measure angular velocity; however, the sensor bias of microelectromechanical system (MEMS) gyroscopes is prone to drift over time. Similarly, electromagnetic interference has an adverse effect on MEMS magnetometers. MEMS accelerometers have stable bias and are resilient to external electromagnetic disturbances. However, they cannot differentiate between gravity and dynamic acceleration [13].

Several methods have been explored for estimating joint angles using noncontact sensors. IMUs fuse sensor data from accelerometers, gyroscopes, and magnetometers using different filtering approaches, including Kalman and complementary filters [14], [15], [16], [17], [18]. Another technique estimates the absolute knee angle and angular velocity by using accelerometers to offset errors that occur from the integration of the angular velocity from the gyroscope [5]. The common-mode rejection (CMR) uses two accelerometers that are mounted on adjacent links to estimate the joint angle. CMR with gyro-integration (CMRG) uses the angular velocity from a gyroscope to help estimate and update the angle. CMR with gyro-differentiation (CMRGD) also uses the angular velocity from a gyroscope, but it differentiates the angular velocity to get the angular acceleration, which is used to estimate the angle. The last method, the distributed CMR (DCMR), uses two asymmetrically placed accelerometers on each link to estimate the joint angle [19]. Building off of these methods is the vestibular dynamic inclinometer (VDI) and the planar VDI (pVDI), which uses two symmetrically placed accelerometers and a gyroscope to measure inclination and joint parameters [20]. This research contributes to this area by formulating the system dynamics by using equivalence of acceleration at the joint, i.e., the acceleration of the joint is the same in coordinate systems of both the links.

Contributions: The research uses an all-accelerometer sensor array on each link comprising two or more accelerometers for joint angle estimation. The system dynamics is constructed using equivalence of acceleration at the joint where the 3-D state vector is the joint angle and angular velocities of the two links. The estimation is performed by using an analytical approach, the extended Kalman filter (EKF) through linearization of the dynamics, and the unscented Kalman filter (UKF) through deterministic sampling. The simulations compare these three approaches and investigate the sensor placement strategies. The estimation noise is shown to be proportional to the mean distance of the sensors and inversely proportional to the relative distance between them. The research investigates the optimal physical placement and number of sensors on each link that minimizes the estimation error. For a given link, the optimal physical placement of the sensors is toward its ends. In addition, it is most desirable to have near-identical sensor placement on both links. The experiments are conducted using three different sensors for four different canonical movements of slow and fast periodic, ramp, and impulse.

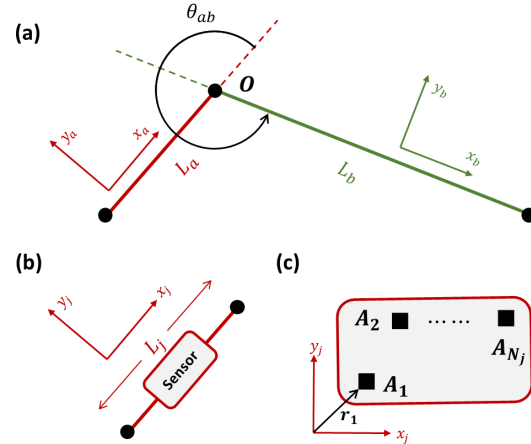


Fig. 1. (a) Two links \$a, b\$ with joint angle \$\theta_{ab}\$ and coordinate system where the \$x\$-axis is along the links. (b) Accelerometer array is placed on each link. (c) Comprises of \$N_j \geq 2\$ accelerometers.

II. DYNAMIC MODEL

Let two links \$a\$ and \$b\$ be joined by revolute joints at \$O\$, as shown in Fig. 1(a). For the link \$j = \{a, b\}\$, let the link reference frame with coordinate system \$\{x_j, y_j, z_j\}\$ (\$z_j\$ out of the plane and \$x_j\$ along the link) rotate with angular velocity and acceleration of \$\omega_j\$ and \$\alpha_j\$. Without loss of generality, the origin of both coordinate systems is assumed to be \$O\$. Assume that \$N_j \geq 2\$ accelerometers are placed along the link \$j\$ at \$r_i, i = 1, \dots, N_j\$, as shown in Fig. 1(b) and (c). It is desired to estimate the joint angle \$\theta_{ab}\$ given the placement of the accelerometers from the joint \$O\$.

Theoretically, the acceleration \$\mathbf{a}_i \in \mathbb{R}^{2 \times 1}\$ of accelerometer \$A_i \forall i \in [1, N_j]\$ is

$$\begin{aligned} \mathbf{a}_i &= \mathbf{a}_O + \boldsymbol{\alpha} \times \mathbf{r}_i + \boldsymbol{\omega} \times (\boldsymbol{\omega} \times \mathbf{r}_i) \\ &= \mathbf{a}_O + D(\mathbf{r}_i) \end{aligned} \quad (1)$$

$$D(\mathbf{r}) = \begin{bmatrix} -r_1 & -r_2 \\ -r_2 & r_1 \end{bmatrix}, \quad \mathbf{y} = \begin{bmatrix} \boldsymbol{\omega}^2 \\ \boldsymbol{\alpha} \end{bmatrix} \quad (2)$$

where \$\mathbf{r} = [r_1, r_2]^T\$, and \$\mathbf{a}_O\$ is the acceleration of point \$O\$. This matrix representation of acceleration of two points on a rigid body is detailed in Appendix I.

A. Sensor Array

Let an array of \$N_j \geq 2\$ accelerometers be placed on a link \$j\$. The \$i\$th accelerometer \$A_i\$ is placed at \$\mathbf{r}_i\$ and measures \$\mathbf{a}'_i\$ such that

$$\mathbf{a}'_i = \mathbf{a}_i + \mathbf{e}_i, \quad \mathbb{E}[\mathbf{e}_i \mathbf{e}_i^T] = Q_i \quad (3)$$

where \$\mathbf{e}_i\$ and \$Q_i\$ are the sensor noise and covariance matrices, respectively. In context of the sensor array, we define acceleration \$\mathbf{a}\$, accelerometer measurement \$\mathbf{a}'\$ and noise \$\mathbf{e}\$ column vectors, and the noise covariance matrix \$Q\$

$$\begin{aligned} \mathbf{a}' &= [\mathbf{a}'_1^T, \mathbf{a}'_2^T, \dots, \mathbf{a}'_{N_j}^T]^T, \quad \mathbf{a} = [\mathbf{a}_1^T, \dots, \mathbf{a}_{N_j}^T]^T \\ \mathbf{e} &= [\mathbf{e}_1^T, \mathbf{e}_2^T, \dots, \mathbf{e}_{N_j}^T]^T, \quad \mathbf{a}', \mathbf{a}, \mathbf{e} \in \mathbb{R}^{2N_j \times 1} \\ Q &= \mathbb{E}[\mathbf{e} \mathbf{e}^T] = \text{diag}(Q_1, \dots, Q_{N_j}), \quad Q \in \mathbb{R}^{2N_j \times 2N_j}. \end{aligned} \quad (4)$$

Let the mean of a set of vectors $\mathbf{v}_k \forall k \in [1, N_j]$ be denoted using an overbar; $\overline{\mathbf{v}} = (1/N_j) \sum_{k=1}^{N_j} \mathbf{v}_k$. We define matrices $F_m, F, G \in \mathbb{R}^{2 \times 2N_j}$, $E \in \mathbb{R}^{2N_j \times 2N_j}$, $D \in \mathbb{R}^{2N_j \times 2}$

$$F_m = \frac{1}{N_j} \begin{bmatrix} \mathbf{1}_2 & \cdots & \mathbf{1}_2 \end{bmatrix}, \quad \text{s.t. } \overline{\mathbf{a}} = F_m(\mathbf{a}' - \mathbf{e}) \quad (5)$$

$$E = \mathbf{1}_{2N_j} - \begin{bmatrix} F_m \\ \vdots \\ \mathbf{1}_2 \end{bmatrix}, \quad \text{s.t. } \widetilde{\mathbf{a}} = E(\mathbf{a}' - \mathbf{e})$$

and

$$\widetilde{\mathbf{a}} = [(a'_1 - \overline{\mathbf{a}})^T, (a'_2 - \overline{\mathbf{a}})^T, \dots, (a'_{N_j} - \overline{\mathbf{a}})^T]^T \quad (6)$$

$$\widetilde{D} = \begin{bmatrix} D(\mathbf{r}_1 - \overline{\mathbf{r}}) \\ D(\mathbf{r}_2 - \overline{\mathbf{r}}) \\ \vdots \\ D(\mathbf{r}_{N_j-1} - \overline{\mathbf{r}}) \end{bmatrix}, \quad \text{s.t. } \widetilde{\mathbf{a}} = \widetilde{D}\mathbf{y} \quad (7)$$

$$G = \widetilde{D}^+ E = \begin{bmatrix} G_{\omega^2} \\ G_a \end{bmatrix}, \quad \text{s.t. } \mathbf{y} = G(\mathbf{a}' - \mathbf{e}) \quad (8)$$

$$F = F_m + D(\overline{\mathbf{r}}_O)G, \quad \text{s.t. } \mathbf{a}_O = F(\mathbf{a}' - \mathbf{e})$$

where

$$\widetilde{\mathbf{r}}_O = \mathbf{r}_O - \overline{\mathbf{r}} \quad (9)$$

where $\mathbf{1}_n$ is the identity of dimension $n \times n$ and \widetilde{D}^+ denotes the pseudoinverse of \widetilde{D} . The reader may also refer to Appendix II for derivations of these matrices. The sensor array must comprise of a minimum of two noncoincident accelerometers to calculate vector \mathbf{y} to ensure that matrix $D(\mathbf{r})$, (2), is full ranked. The reader may refer to [21] for a generic proof for the requirement of minimum accelerometers in an array.

B. System Dynamics

Proposition 1: For two links $\{a, b\}$ joined by a revolute joint where each link has an accelerometer sensor array, the continuous-discrete time dynamical model with states $\mathbf{x} = [\omega^a, \omega^b, \theta_{ab}]^T$ is

$$\dot{\mathbf{x}} = f(\mathbf{x}) + \mathbf{w}$$

$$\mathbf{z} = h(\mathbf{x}) + \mathbf{v}, \quad \text{s.t. } f(\mathbf{x}) = (Ax + B\widehat{\mathbf{a}}) \quad (10)$$

$$A = \begin{bmatrix} 0 & 0 & 0 \\ 0 & 0 & 0 \\ 1 & -1 & 0 \end{bmatrix}, \quad B = \begin{bmatrix} G_a^a & 0 \\ 0 & G_a^b \\ 0 & 0 \end{bmatrix}, \quad \mathbf{w} = B\widehat{\mathbf{e}}$$

$$\mathbf{z} = Z\widehat{\mathbf{a}}, \quad Z = \begin{bmatrix} G_{\omega^2}^a & 0 \\ 0 & G_{\omega^2}^b \\ F^a & 0 \end{bmatrix}, \quad \mathbf{v} = V\widehat{\mathbf{e}}$$

$$V = \begin{bmatrix} G_{\omega^2}^a & 0 \\ 0 & G_{\omega^2}^b \\ F^a & -R(x_3)F^b \end{bmatrix}, \quad h(\mathbf{x}) = \begin{bmatrix} x_1^2 \\ x_2^2 \\ R(x_3)F^b \mathbf{a}'^b \end{bmatrix} \quad (11)$$

where $\widehat{\mathbf{a}} = [(\mathbf{a}'^a)^T, (\mathbf{a}'^b)^T]^T$, $\widehat{\mathbf{e}} = [(\mathbf{e}^a)^T, (\mathbf{e}^b)^T]^T \in \mathbb{R}^{4N_j \times 1}$, and $\mathbf{z}, h(\mathbf{x}) \in \mathbb{R}^{3 \times 1}$. The superscripts denote the quantity corresponding to link a or b .

Proof: The vector \mathbf{y} from (8) contains information about angular acceleration and the square of angular velocity. For

the state \mathbf{x}

$$\dot{\mathbf{x}} = \begin{bmatrix} \omega^a \\ \omega^b \\ \theta_{ab} \end{bmatrix} = \begin{bmatrix} G_a^a(\mathbf{a}'^a - \mathbf{e}^a) \\ G_a^b(\mathbf{a}'^b - \mathbf{e}^b) \\ \omega^a - \omega^b \end{bmatrix} = \underbrace{Ax + B\widehat{\mathbf{a}}}_{f(\mathbf{x})} + \underbrace{B\widehat{\mathbf{e}}}_{\mathbf{w}}.$$

The three rows of the measurement vector correspond to the square of the angular velocities $(\omega^a)^2, (\omega^b)^2$ and the equivalence of the acceleration at the joint, i.e., $\mathbf{a}_O^a = R(\theta_{ab})\mathbf{a}_O^b$. Consequently,

$$\begin{aligned} z_1 &= G_{\omega^2}^a \mathbf{a}'^a = (\omega^a)^2 + G_{\omega^2}^a \mathbf{e}^a \\ z_2 &= G_{\omega^2}^b \mathbf{a}'^b = (\omega^b)^2 + G_{\omega^2}^b \mathbf{e}^b \\ \underbrace{F^a(\mathbf{a}'^a - \mathbf{e}^a)}_{\mathbf{a}_O^a} &= R(\theta_{ab}) \underbrace{F^b(\mathbf{a}'^b - \mathbf{e}^b)}_{\mathbf{a}_O^b} \\ \Rightarrow z_3 &= F^a \mathbf{a}'^a = R(\theta_{ab}) F^b \mathbf{a}'^b \\ &\quad + (F^a \mathbf{e}^a - R(\theta_{ab}) F^b \mathbf{e}^b) \\ \Rightarrow \mathbf{z} &= Z\widehat{\mathbf{a}} = h(\mathbf{x}) + V\widehat{\mathbf{e}}. \end{aligned} \quad \blacksquare$$

III. JOINT ANGLE AND ANGULAR VELOCITY ESTIMATION

We examine the joint angle and angular velocity estimation using three approaches: analytical, EKF, and UKF.

A. Analytical Joint Angle Estimate

For a vector \mathbf{v} , the rotation matrix (Lie group of joint angle θ_{ab}) defines the relationship between its representation in two coordinate systems $\{a, b\}$

$$\mathbf{v}^a = R(\theta_{ab})\mathbf{v}^b, \quad \text{s.t. } R(\theta) = \begin{bmatrix} c_\theta & s_\theta \\ -s_\theta & c_\theta \end{bmatrix}$$

and

$$\theta_{ab} = \text{atan2}\left(v_1^a v_2^b - v_2^a v_1^b, v_1^a v_1^b + v_2^a v_2^b\right) \quad (12)$$

where superscript denotes the coordinate system of representation and atan2 is the two-argument arctangent. Geometrically, (12) is the cross product (sine) and dot product (cosine) of the two vectors. For the current scenario, the acceleration at the joint O is the vector \mathbf{v} in (12) that is calculated using the sensor arrays on the links using (9). However, this approach will be adversely affected by the noise from the accelerometers. This approach is similar to CMR discussed in [19].

B. Extended Kalman Filter

The continuous-discrete time system is discretized and linearized to construct the EKF. We use the [22] notation to enable ease of understanding

$$\begin{aligned} \mathbf{x}_k &= \mathbf{x}_{k-1} + f(\mathbf{x}_{k-1})\Delta T + \mathbf{w}_{k-1} \\ &= (\mathbf{I}_3 + A\Delta T)\mathbf{x}_{k-1} + \Delta T B\widehat{\mathbf{a}} + \Delta T B\widehat{\mathbf{e}} \end{aligned} \quad (13)$$

$$\begin{aligned} \mathbf{z}_k &= h(\mathbf{x}_k) + \mathbf{v}_k \\ &= h(\mathbf{x}_k) + V\widehat{\mathbf{e}} \end{aligned} \quad (14)$$

where ΔT is the sample time, and the Jacobians and the noise covariance matrices are

$$H(\mathbf{x}) = \frac{\partial h(\mathbf{x})}{\partial \mathbf{x}} = \begin{bmatrix} 2x_1 & 0 & 0 \\ 0 & 2x_2 & 0 \\ 0 & 0 & R'(x_3)F^b \mathbf{a}'^b \end{bmatrix} \quad (15)$$

$$F(\mathbf{x}) = \frac{\partial f(\mathbf{x})}{\partial \mathbf{x}} = \mathbf{1}_3 + A \Delta T \quad (16)$$

$$Q_k = \mathbb{E}[\mathbf{w}_{k-1}\mathbf{w}_{k-1}^T] = \Delta T^2 B \widehat{Q} B^T \quad (17)$$

$$R_k = \mathbb{E}[\mathbf{v}_k\mathbf{v}_k^T] = V \widehat{Q} V^T \quad (18)$$

where

$$\widehat{Q} = \mathbb{E}[\tilde{\mathbf{e}}\tilde{\mathbf{e}}^T] = \text{diag}(Q^a, Q^b)$$

where

$$Q^j = \mathbb{E}[(\mathbf{e}^j)(\mathbf{e}^j)^T] \quad \forall j = \{a, b\}. \quad (19)$$

The EKF is implemented in a recursive fashion assuming P_0 and x_0 at $t = 0$. For every time step $k \geq 1$, the following holds.

1) Time Update:

$$\begin{aligned} \bar{\mathbf{x}}_k &= f(\mathbf{x}_{k-1}) \\ P_k^- &= F(\mathbf{x}_{k-1})P_{k-1}F(\mathbf{x}_{k-1})^T + Q_k. \end{aligned}$$

2) Measurement Update:

$$\begin{aligned} K_k &= P_k^- H(\bar{\mathbf{x}}_k)^T (H(\bar{\mathbf{x}}_k)P_k^- H(\bar{\mathbf{x}}_k)^T + R_k)^{-1} \\ \mathbf{x}_k &= \bar{\mathbf{x}}_k + K_k(z - h(\bar{\mathbf{x}}_k)) \\ P_k &= (I - K_k H(\bar{\mathbf{x}}_k))P_k^-. \end{aligned}$$

The Kalman filter makes the assumption of uncorrelated process-measurement noise [22]. Here, it is easy to observe that the assumption does not hold true for this case, where $\mathbb{E}[\mathbf{w}\mathbf{v}^T] \neq \mathbf{0}_{3 \times 4}$. However, process dynamics can be modified to

$$\dot{\mathbf{x}} = \tilde{f}(\mathbf{x}) + \tilde{\mathbf{w}}$$

where

$$\begin{aligned} \tilde{f}(\mathbf{x}) &= f(\mathbf{x}) - L(z - h(\mathbf{x})) \\ \tilde{\mathbf{w}} &= \mathbf{w} - Lv, \quad \text{s.t. } \mathbb{E}[\tilde{\mathbf{w}}\mathbf{v}^T] = 0 \\ \Rightarrow L &= (\mathbb{E}[\mathbf{w}\mathbf{v}^T]) (\mathbb{E}[\mathbf{v}\mathbf{v}^T])^{-1}. \end{aligned} \quad (20)$$

C. Unscented Kalman Filter

In the previously described EKF, the Gaussian random variable (GRV) is analytically propagated through first-order linearization of the nonlinear system dynamics. This may introduce large errors in the mean and covariance of the posterior. The UKF addresses this problem by using a deterministic sampling approach [23], [24]. The proposed approaches by Julier and Uhlmann [23] and Wan and Van Der Merwe [24] completely capture the mean and covariance accurately to the third order (Taylor series expansion) for any nonlinearity. The number of points sampled is $(2n + 1)$, where n is the dimension of the state vector; here, $n = 3$. For a given

mean $\bar{\mu}$ and covariance Σ , the seven sampled points $\chi_i = \text{sampleSigmaPoints}(\bar{\mu}, \Sigma)$ are

$$\begin{aligned} \chi_0 &= \bar{\mu} \\ \chi_{i,n+i} &= \bar{\mu} \pm \text{col}_i \left(\sqrt{(n + \lambda)\Sigma} \right) \quad \forall i = 1, \dots, n \end{aligned} \quad (21)$$

where λ is the scaling parameter. The associated mean and covariance weights, $w_i^{[m]}$ and $w_i^{[c]}$, corresponding to each sigma points are

$$\begin{aligned} w_0^{[m]} &= \frac{\lambda}{n + \lambda}, \quad w_0^{[c]} = w_m^{[0]} + (1 - \alpha^2 + \beta) \\ w_i^{[m]} &= w_i^{[c]} = \frac{1}{2(n + \lambda)} \quad \forall i = 1, \dots, 2n \\ \beta &= 2, \quad \alpha \in (0, 1], \quad \lambda = \alpha^2(n + \kappa) - n, \quad \text{s.t. } \kappa \geq 0. \end{aligned} \quad (22)$$

Here, the UKF can be tuned using different values of κ and α with optimal $\beta = 2$ for Gaussian distributions. Similar to the EKF, the UKF is implemented in a recursive manner assuming P_0 and x_0 at $t = 0$ and using (13), (14), (17), and (18). For every time step $k \geq 1$, the following holds.

1) Time Update:

$$\begin{aligned} \bar{\mathbf{x}}_k &= \text{sampleSigmaPoints}(\mathbf{x}_{k-1}, P_{k-1}) \\ \bar{\mathbf{x}}_k &= \sum_{i=0}^{2n} w_i^{[m]} g(\chi_i^-), \quad \text{where } g(\mathbf{x}) = \mathbf{x} + f(\mathbf{x})\Delta T \\ P_k^- &= \sum_{i=0}^{2n} w_i^{[c]} (g(\chi_i^-) - \bar{\mathbf{x}}_k) (g(\chi_i^-) - \bar{\mathbf{x}}_k)^T + Q_k. \end{aligned}$$

2) Measurement Update:

$$\begin{aligned} \chi_i &= \text{sampleSigmaPoints}(\bar{\mathbf{x}}_k, P_k^-) \\ h_k &= \sum_{i=0}^{2n} w_i^{[m]} h(\chi_i), \\ P_{z_k, z_k} &= \sum_{i=0}^{2n} w_i^{[c]} (h_k - h(\chi_i)) (h_k - h(\chi_i))^T + R_k \\ P_{x_k, z_k} &= \sum_{i=0}^{2n} w_i^{[c]} (\chi_i - \bar{\mathbf{x}}_k) (h(\chi_i) - z_k)^T \\ \mathbf{x}_k &= \bar{\mathbf{x}}_k + K_k(z_k - h_k), \quad K_k = P_{x_k, z_k} P_{z_k, z_k}^{-1} \\ P_k &= P_k^- - K_k P_{z_k, z_k} K_k^T. \end{aligned}$$

Concisely, the process samples the data points during both the time and measurement update and does not require the calculation of the Jacobians F_k and H_k . The system dynamics are modified using (20) when the process-measurement noise is correlated. Table I summarizes the nomenclature for the system and filter parameters along with their respective dimensions.

IV. SIMULATION

The simulation of movement and estimation of the joint angle was performed to investigate the performance of the three aforementioned approaches and the impact of sensor placement on the estimation error. Movement of a planar

TABLE I
SUMMARY OF NOMENCLATURE OF THE SYSTEM AND FILTER PARAMETERS

	Variable	Description	Dimension
Sensor Array	N_j	Number of accelerometers on link j	\mathbb{Z}
	\mathbf{a}' or \mathbf{a}'^j	Cumulative measured accelerations of link j	$\mathbb{R}^{2 \times 2N_j}$
	$\hat{\mathbf{a}}$	Cumulative measured accelerations of links a and b	$\mathbb{R}^{2 \times 2(N_a+N_b)}$
	\hat{Q}	Cumulative covariance of accelerometers on links a and b	$\mathbb{R}^{2(N_a+N_b) \times 2(N_a+N_b)}$
	\tilde{D}	Cumulative relative displacement matrix D	$\mathbb{R}^{2N_j \times 2}$
	G	Accelerometer-angular parameter transformation matrix	$\mathbb{R}^{2 \times 2(N_j)}$
	F	Accelerometer-joint acceleration transformation matrix	$\mathbb{R}^{2 \times 2(N_j)}$
System Dynamics	Z	Acceleration-measurement transformation matrix	$\mathbb{R}^{4 \times 2(N_a+N_b)}$
	\mathbf{x}_k	State vector	\mathbb{R}^3
	\mathbf{z}_k	Measurement vector	\mathbb{R}^4
	$F(x_k)$	State transition matrix	$\mathbb{R}^{3 \times 3}$
	B	Input matrix	$\mathbb{R}^{3 \times 2(N_a+N_b)}$
	$h(x_k)$	Measurement model	\mathbb{R}^4
	$H(x_k)$	Jacobian of the measurement model	$\mathbb{R}^{4 \times 4}$
Filter Parameters	V	Measurement error matrix	$\mathbb{R}^{4 \times 2(N_a+N_b)}$
	Q_k	State noise covariance matrix	$\mathbb{R}^{3 \times 3}$
	R_k	Measurement noise covariance matrix	$\mathbb{R}^{4 \times 4}$
	P_k	Estimation error covariance matrix	$\mathbb{R}^{3 \times 3}$
	K_k	Kalman gain	$\mathbb{R}^{3 \times 4}$
	P_{x_k, z_k}	Cross covariance matrix	$\mathbb{R}^{3 \times 4}$
	P_{z_k, z_k}	Innovation covariance matrix	$\mathbb{R}^{4 \times 4}$

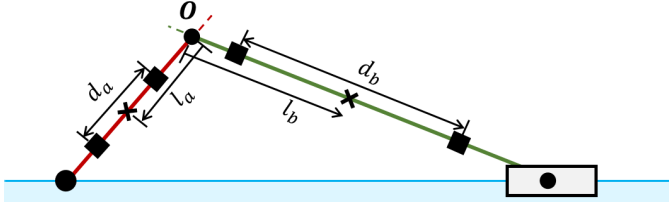


Fig. 2. Slider crank mechanism used for simulating joint angle dynamics. Two accelerometers are placed at mean and relative distances of l_j , d_j on each of the links, $j = a, b$.

slider-crank mechanism (see Fig. 2) was modeled to simulate dynamic movement of links a and b . The true angular velocity and acceleration of the links, joint angle, and linear acceleration of the accelerometers were calculated using the mechanism dynamics, as detailed in Appendix III. The accelerometers were assumed to have white Gaussian noise with a power density of $400 \mu\text{g}/\sqrt{\text{Hz}}$ and a sampling frequency of 100Hz . Without loss of generality, two accelerometers were placed on each link at

$$\bar{\mathbf{r}}_i = \left[\frac{l_i}{2}, 0 \right]^T, \quad \mathbf{r}_{j,i} = \bar{\mathbf{r}} \pm \left[\frac{d_i}{2}, 0 \right]^T \quad \forall i = a, b; \quad j = 1, 2.$$

All simulations were performed in MATLAB.¹ l_i and d_i are the mean and relative lengths of the accelerometers, respectively.

The noise used for each simulation was randomized; hence, Q_k and R_k were reevaluated for each simulation. An example

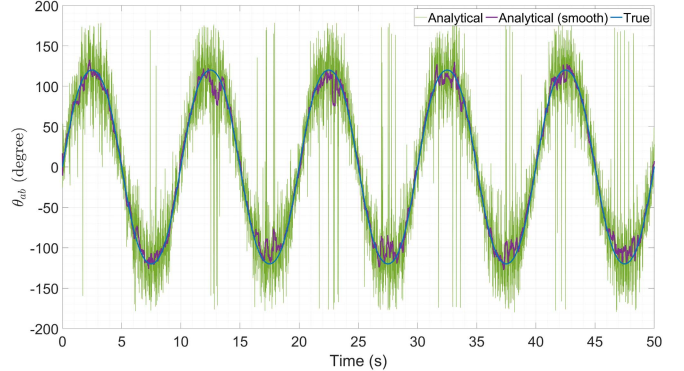


Fig. 3. Comparison of analytical θ_{ab} with smoothing over a window.

$\hat{Q} \in \mathbb{R}^{8 \times 8}$ matrix used for calculation of Q_k and R_k is

$$\hat{Q} = \text{diag}(5, 7, 2.9, 4.6, 19, 13.4, 8.8) \times 10^{-3}.$$

In addition, the initial state and estimation error covariance matrices were

$$\mathbf{x}_0 = [0, 0, 0]^T, \quad P_0 = \mathbf{1}_3.$$

In the first scenario, accelerometers are placed at $l_a = l_b = 5 \text{ cm}$ and $d_a = d_b = 5 \text{ cm}$ for $L = 10 \text{ cm}$ and $L_a = L, L_b = 2L$ long links. As evident from (12), the sensor noise has an adverse effect on the calculation of the analytical joint angle. This can be mitigated by smoothing the signal at the cost of sensing delay, i.e., moving average of the data. For a window of 25 data points, the smoothing filter provides better results, as shown in Fig. 3. Hereafter, the smooth-analytical solution was used for visual comparison of EKF and UKF approaches.

¹Registered trademark.

TABLE II

COMPARISON OF THE RMS ERROR IN ESTIMATES FOR CHANGE IN THE DISTANCE BETWEEN THE ACCELEROMETERS

	L (cm)	$l = d$ (cm)	Analytical	Smooth Analytical	UKF	EKF
θ_{ab}	30	15	9.04°	1.74°	1.21°	0.71°
	20	10	13.69°	2.77°	1.41°	1.79°
	10	5	41.42°	10.32°	3.35°	3.12°
ω_a	30	15	X	X	3.96°/s	0.69°/s
	20	10	X	X	4.10°/s	1.10°/s
	10	5	X	X	4.49°/s	2.21°/s
ω_b	30	15	X	X	2.07°/s	0.97°/s
	20	10	X	X	2.40°/s	1.55°/s
	10	5	X	X	3.49°/s	3.11°/s

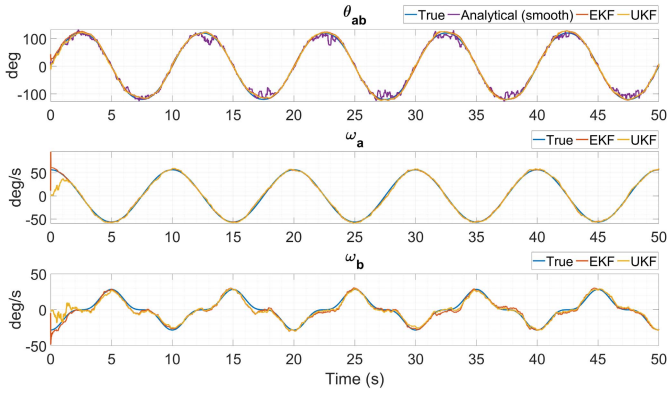


Fig. 4. Comparison of joint angle and angular velocities of the simulated slider-crank mechanism. The analytical solution only estimates the joint angle, while EKF and UKF approaches also estimate the joint velocity.

When comparing the three approaches, the model-based filters (EKF and UKF) show more promise than the analytical approach, as shown in Fig. 4. The analytical, smooth-analytical, EKF, and UKF estimate root mean square (rms) errors for θ_{ab} were 41.42°, 10.32°, 3.12°, and 3.35°, respectively. Unlike EKF and UKF, the smoothing operation introduces an estimation delay depending upon the smoothing window.

The placement of the sensors, mean, and relative lengths $\{l_a, l_b, d_a, d_b\}$ have direct impact on the estimation error. However, the exploration of such a huge parameter space is unfeasible. For the scenario where the relative to mean length ratios are kept constant as one, the variation in the estimation error is tabulated in Table II. Here, the error decreases with an increase in the lengths d or l . The results also show that the EKF and UKF perform better compared to analytical (smooth). In addition, UKF performs better as lengths decrease; however, overall, the performances are similar. Importantly, unlike the analytical approach, the two estimation algorithms also estimate angular velocity.

As discussed in Section III, the estimation approach is applicable for a sensor array comprising more than two accelerometers on each link (see Section II-A). Consequently, the optimal number of accelerometers per link is investigated by varying the number of sensors in the array. Here, the N_i accelerometers are placed uniformly along the link $i = \{a, b\}$ such that the j th accelerometer is at

$$\bar{\mathbf{r}}_i = \left[\frac{l_i}{2}, 0 \right]^T, \quad \mathbf{r}_{j,i} = \bar{\mathbf{r}} \pm \frac{(j-1)}{(N_i - 1)} \left[\frac{d_i}{2}, 0 \right]^T \quad \forall j = 1, \dots, N_i$$

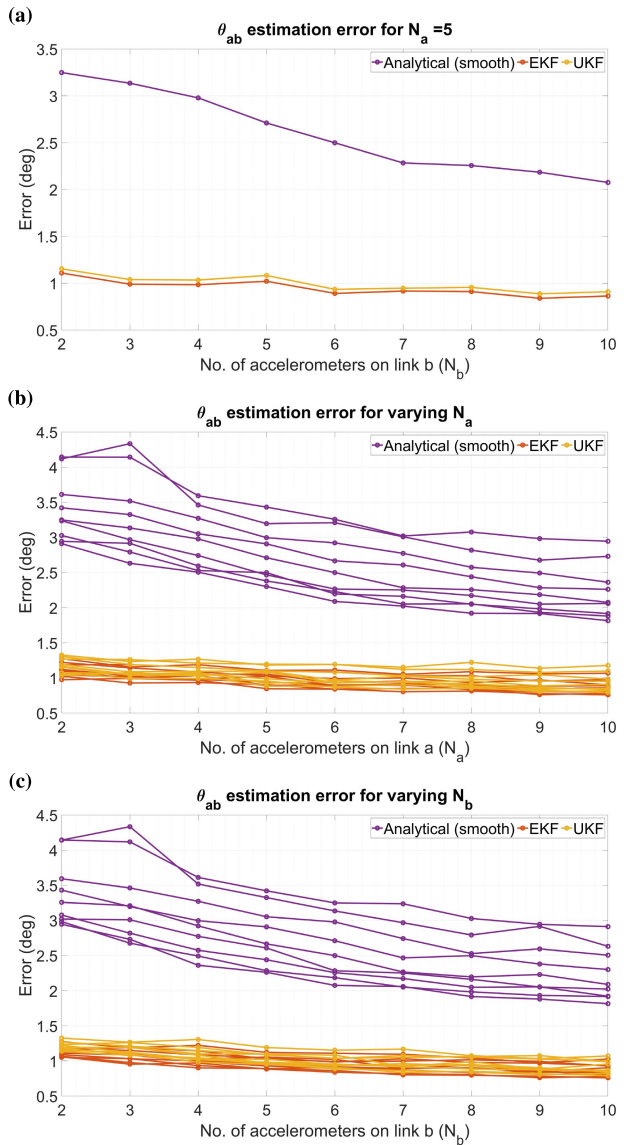


Fig. 5. Estimation error for change in the number of accelerometers. (a) $N_a = 5$, while N_b is varied. (b) Cumulative plot for $N_a = 2, \dots, 10$ for variation in N_b . Here, each line corresponds to N_b between two and ten. (c) Cumulative plot for all N_b as N_a is varied. Each line corresponds to N_a between two and ten.

Simulation is performed on a slider-crank with $L_a = 20$ cm and $L_b = 25$ cm with the mean and relative lengths of $l_a = l_b = d_a = d_b = 10$ cm. The number of accelerometers on each link, N_a and N_b , is varied from two to ten. The error in estimation of the joint angle θ_{ab} is observed for change in N_a and N_b . Fig. 5(a) plots the estimation error $N_a = 5$ as N_b is varied. Fig. 5(b) and (c) cumulatively observes the error as both N_a and N_b are varied. Here, each line corresponds to the number of accelerometers on the link. The simulation results indicate that an additional number of accelerometers N_a and $N_b > 2$ are slightly beneficial for the analytical method; however, the filtering approaches (EKF and UKF) minimally benefit from the extra sensory information.

For the next scenario, the estimation error was evaluated for change in l_b and d_b for constant mean to relative length ratio of link a , i.e., l_a/d_a . The remainder of the analysis was performed on a slider-crank mechanism with link lengths $L_a = 20$ cm and $L_b = 200$ cm with the mean and relative lengths

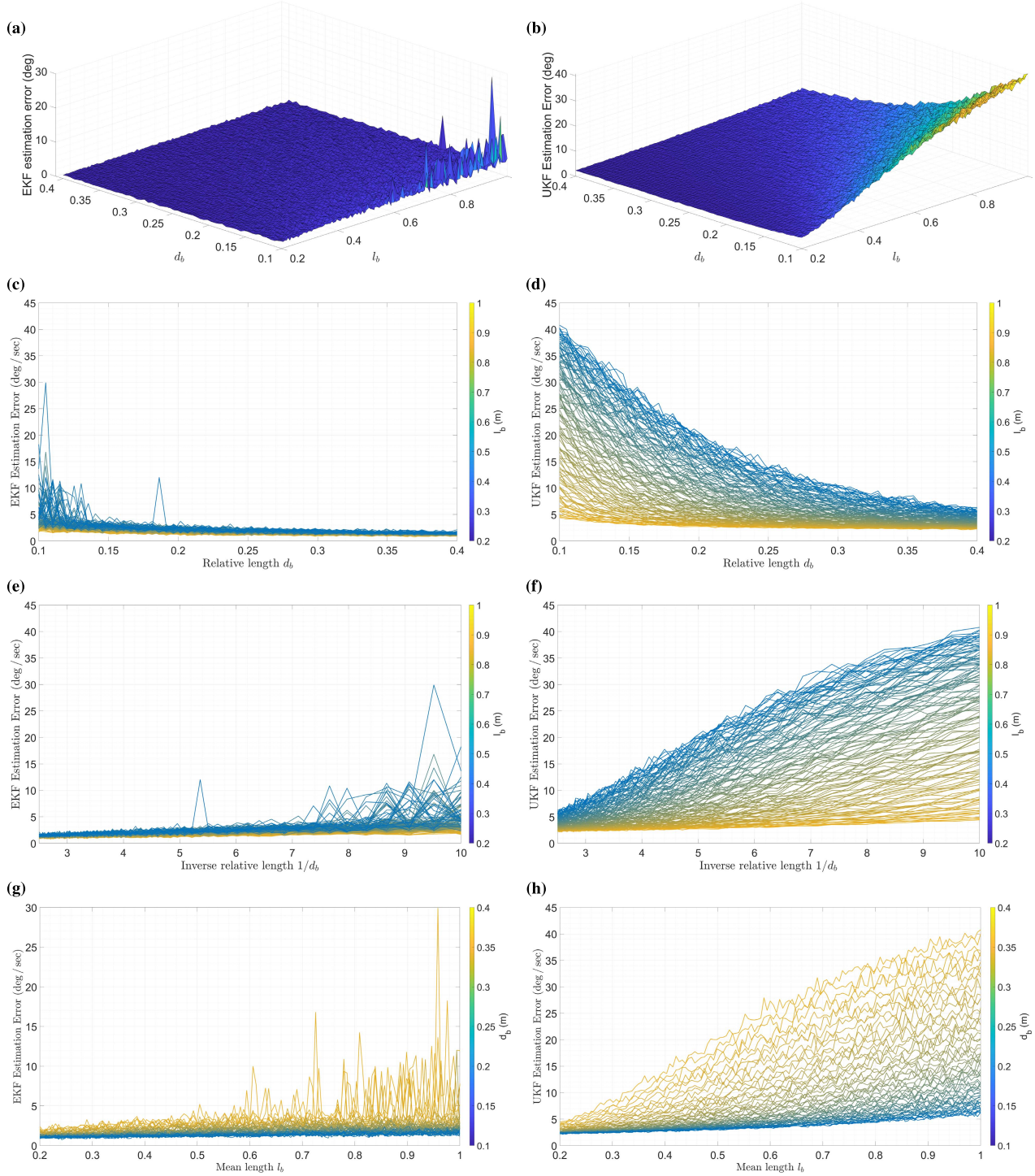


Fig. 6. Estimation errors for (a) and (b) EKF and UKF as relative and mean lengths of link b are varied for $l_a = d_a = 10$ cm. (c) and (d) Side views of the plot to observe change in error for all l_b as d_b is varied. (e) and (f) Linear relationship between $1/d_b$ and estimation error for a given l_b . (g) and (h) Linear relationship between l_b and the error for given d_b .

of $l_a = d_a = 10$ cm. Fig. 6(a) and (b) plots the EKF and UKF estimation errors as the mean and relative lengths of link b are varied. Fig. 6(c) and (d) shows the side plots of these surface plots where each line color corresponds to l_b varying between 20 and 100 cm. The inverse relationship between estimation error and d_b for any given l_b [see Fig. 6(e) and (f)] suggests that a larger value of d_b is desirable, while Fig. 6(g) and (h) indicates a linear relationship of the error with l_b for any given d_b . Consequently, for a physical link of length L_b , the optimal

placement of the accelerometers, d_b^* and l_b^* , is as close to the ends of the link as possible

$$d_a^* \rightarrow L_a, \quad l_a^* = \frac{L_a}{2} \Rightarrow \left(\frac{l_a}{d_a}\right)^* \rightarrow \frac{1}{2}. \quad (23)$$

The effect of change in mean to relative length of link a was examined in Fig. 7 for $l_a/d_a = 0.5, 1, 2, 5$. Here, each color plot includes a variation of l_b from 20 to 100 cm, i.e., same as the previous analysis but with the same color rather than

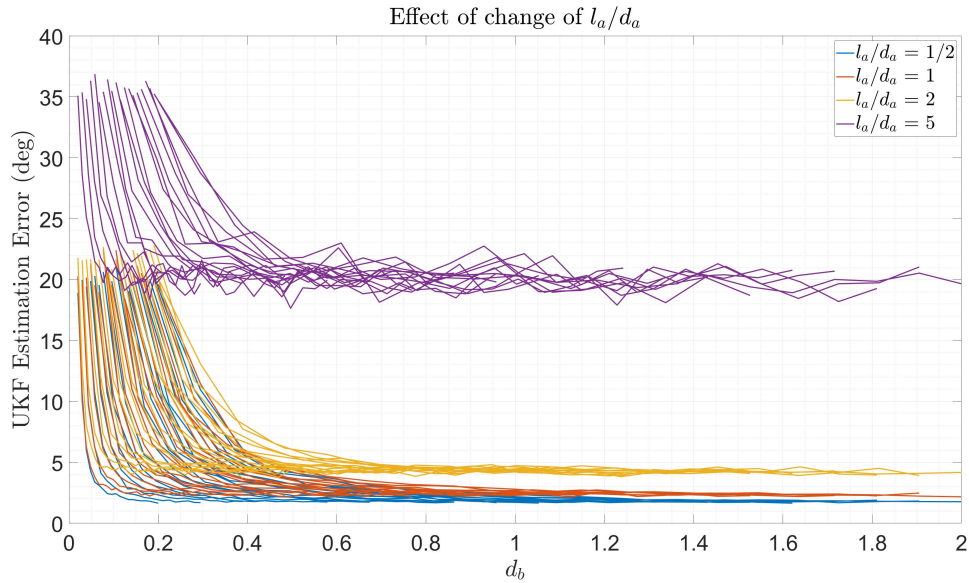


Fig. 7. Estimation error as mean to relative length ratio for link a is varied. Each color line corresponds to l_b between 20 and 100 cm. The lower bound of achievable estimation error is dictated by the l_a/d_a ratio.

color variation. The analysis indicates that, irrespective of the increase in d_b , the lower bound of the error estimate (achievable minimum error) is dictated by the l_a/d_a ratio and the parameters of link a . Concisely, near identical sensor placement, i.e., $l_a/d_a \approx l_b/d_b$, is most desirable between two links.

V. EXPERIMENTS AND RESULTS

The experimental setup comprised of two links of 30 cm joined by a revolute joint. A US Digital MA3 absolute magnetic shaft encoder was placed at the joint to measure the true angle. One of the links was clamped to a solid surface for purpose of stability. Each link had two accelerometers mounted on it at distances of 4.75 and 27.5 cm from the joint, as visualized in Fig. 8(a). The mechatronics for acquiring and processing the sensor data comprised of an Arduino Mega and multiplexer serially connected to the computer. The sensors communicate with the microprocessor through the I2C protocol.

The accelerometers were calibrated using the least squares approach discussed in Appendix IV. The link coordinate systems were defined such that the x -axis is along the link and the z -axis out of the plane of the paper. Seven different calibration poses were chosen where the link x - and y -axes align along $\pm g$ of gravity, as detailed in Fig. 8(b).

Four canonical movements were identified to test the algorithms: “slow periodic” refers to slow and continuous back-and-forth movement, “fast periodic” as fast sinusoidal movements, “ramp” for slow movement with pauses, and “impulse” as fast, sudden movements with pauses. The joint angle for the four aforementioned canonical movements is illustrated in Fig. 9. Here, the EKF and UKF estimates are very close, and their plots (mustard and purple lines) overlap.

Experimental verification was performed on three different sensors, ADXL345, ADXL357, and BNO055, as illustrated in Fig. 9. On average, the ADXL345 performed the best; however, both BNO055 and ADXL345 had the smallest sensing range of 2 g, whereas the ADXL357 was set at a sensing range of 10 g. The estimation errors for the canonical

TABLE III
EXPERIMENTAL RESULTS (RMS ERROR OF THE JOINT ANGLE) FOR THE THREE ALGORITHMS USING THREE DIFFERENT SENSORS

Canonical Movement	Algorithm	ADXL345	ADXL357	BNO055
Slow Periodic	Analytical	3.61°	4.70 °	4.00°
	EKF	3.09°	4.80°	4.14°
	UKF	3.03°	4.8°	4.11°
Fast Periodic	Analytical	6.41°	11.13°	9.99°
	EKF	5.50°	9.45°	3.48°
	UKF	5.51°	9.47°	3.5°
Ramp	Analytical	4.45°	7.13 °	2.99°
	EKF	4.21°	6.87°	3.47°
	UKF	4.18°	6.88°	3.45°
Impulse	Analytical	11.67°	11.39 °	17.72°
	EKF	7.95°	11.42°	10.52°
	UKF	7.92°	11.37°	10.51°

movements are tabulated in Table III. The experimental errors are larger than observed for simulation. These are hypothesized to be due to systematic errors, e.g., accelerometer calibration and sensor placement measurement. The sensors must be calibrated more precisely, or sensors with less noise may be used for reducing estimation errors. Between the three different sensors, 100 experiments were performed to examine the repeatability of the proposed methods. The results were consistent where the accelerometer calibration had a direct effect on the estimation error. This highlighted the critical nature of sensor calibration. The EKF and UKF had very similar performances, where the UKF algorithm did not require additional linearization. They marginally outperformed the analytical smoothing method and had better results for fast movements. The Kalman filtering algorithms bring more accuracy to the joint angle measurement and also provide an estimate of the angular velocity that is not available with the analytical (smooth) algorithm. The additional computational complexity is justified for applications where the movements are fast, and there is a requirement of link angular velocities, e.g., biomechanics. However, for potential applications where there is a slow change in joint angle, the analytical-smooth approach may be sufficient.

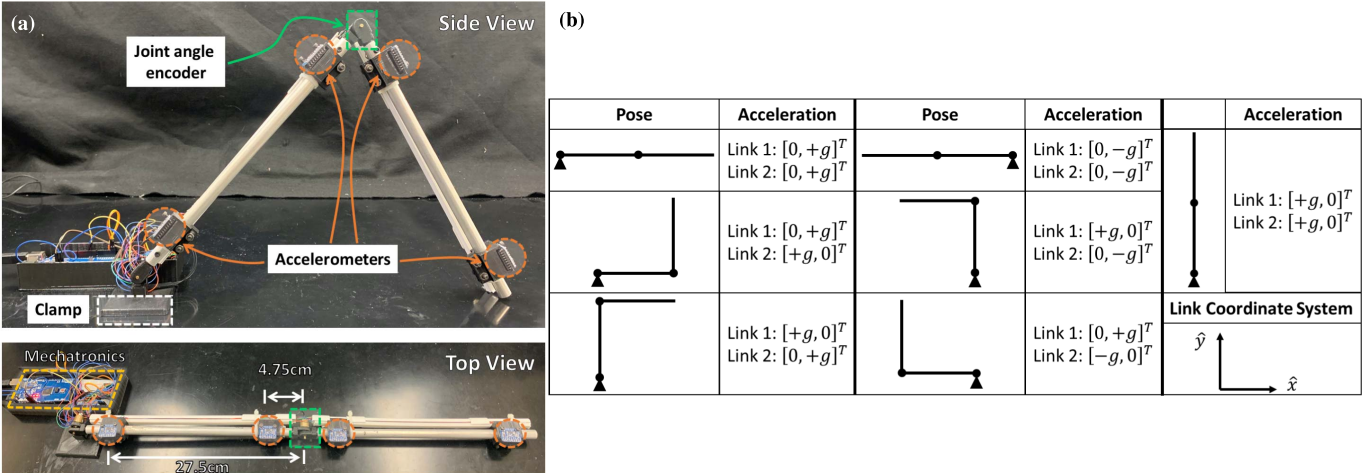


Fig. 8. (a) Experimental setup comprised of two links joined by a magnetic encoder. The accelerometers were placed at 4.75 and 27.5 cm from the joint. (b) Seven poses used for calibrating the accelerometers where the axes of the sensors align along the positive and negative directions of gravity.

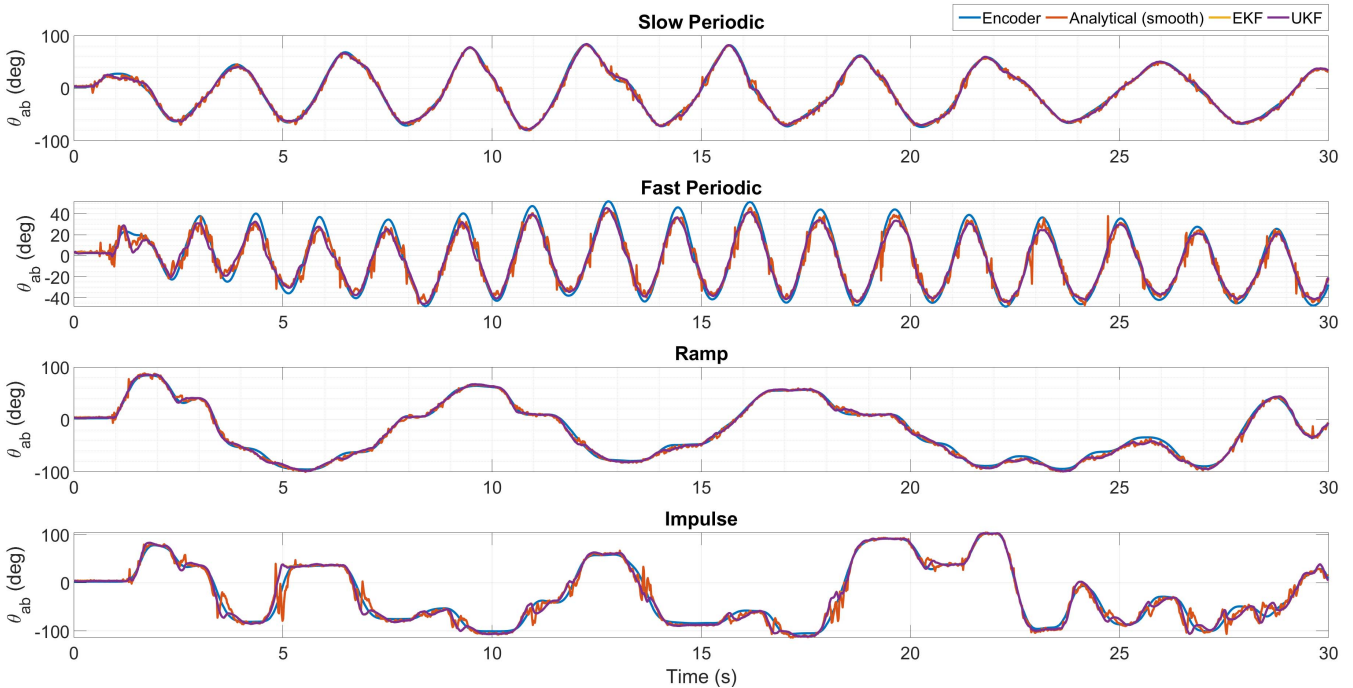


Fig. 9. Comparison of joint angle and angular velocities of experimental two-link mechanism. The analytical solution only estimates the joint angle, while EKF and UKF approaches also estimate the joint velocity.

Theoretically, the use of EKF or UKF is application-specific where aspects such as nonlinearity of the system dynamics and sampling frequency need to be considered. For symbolically complex state transition and measurement models, the UKF is advantageous as the Jacobians need not be analytically calculated. For the joint angle estimation application, the computational complexities of both EKF and UKF are similar given the processing power of modern-day computers. Given the availability of symbolic Jacobian, the use of EKF provides a slight advantage. However, the choice between the two methods is not expected to provide stark differences.

Considering state-of-the-art techniques for joint angle estimation, researchers use gyroscopes and magnetometers in addition to accelerometers. El-Gohary and McNames [6], [7] use an EKF and UKF for joint angle estimation using

three IMUs and reduce the drift by modeling the sensor bias. Their estimation errors are between 0.9° and 9.7° . Weygers *et al.* [16] also use an accelerometer-gyroscope combination and obtain knee joint estimation errors of 1.85° - 3.66° , while Cooper *et al.* [17] use EKF on an accelerometer-gyroscope combination to obtain knee joint error between 0.7° and 3.4° .

VI. CONCLUSION

The research uses an all-accelerometer sensor setup for joint angle estimation. The presented system dynamics are valid for an accelerometer array of two or more sensors on each link. Three estimation approaches are presented—analytical, EKF, and UKF. Apart from the joint angle, the Kalman filtering approaches also estimate the angular velocity of the

links. Unlike the EKF, UKF does not require linearization and uses deterministic sampling. The simulation is performed using a slider-crank mechanism and proves the viability of the approach. Here, the EKF and UKF performances were similar and superior to the analytical (smooth). The optimal sensor placement strategy is explored by varying the mean and relative length of accelerometer positions. The analyses conclude that, for a given link, the best physical placement of the sensors is toward the end of the link. In addition, between two links, the higher ratio of mean to relative accelerometer position defines the maximum achievable accuracy of the system. The optimal number of accelerometers per link is also investigated. The simulation results indicate that more than two accelerometers per link may be slightly beneficial for the analytical method. However, it has minimal influence on the filtering approaches (EKF and UKF). Experimentally, three different sensors are tested—ADXL345, ADXL357, and BNO055 with the three different methods. The experiments were performed on four unique canonical movements of slow and fast periodic, ramp, and impulse. The experiments validate the simulation results of better EKF and UKF performance in comparison to analytical. However, with more precise sensors and effective calibration techniques, the accuracy of filtering estimates can be further improved.

APPENDIX I

MATRIX REPRESENTATION OF ACCELERATION OF TWO POINTS ON A RIGID BODY

Acceleration of any two points O and P on a rigid body is [25]

$$\mathbf{a}_P = \mathbf{a}_O + \boldsymbol{\alpha} \times \mathbf{r}_i + \boldsymbol{\omega} \times (\boldsymbol{\omega} \times \mathbf{r}_i)$$

where all the quantities are expressed in the body coordinate system. In the context of the current research, the rigid body is the link, and point P corresponds to the accelerometer position. For a vector $\mathbf{v} = [v_1, v_2, v_3]^T$, the cross product can be written in matrix form as

$$\mathbf{v} \times = \begin{bmatrix} 0 & -v_3 & v_2 \\ v_3 & 0 & -v_1 \\ -v_2 & v_1 & 0 \end{bmatrix}.$$

Hence, for the planar case where $\boldsymbol{\omega}$, $\boldsymbol{\alpha}$ are out of the plane of the paper and $\mathbf{r}_P = [r_{1,P}, r_{2,P}]^T$ is in the xy plane

$$\boldsymbol{\omega} \times = \begin{bmatrix} 0 & -\omega \\ \omega & 0 \end{bmatrix}, \quad (\boldsymbol{\omega} \times)^2 = \begin{bmatrix} -\omega^2 & 0 \\ 0 & \omega \end{bmatrix}, \quad \boldsymbol{\alpha} \times = \begin{bmatrix} 0 & -\alpha \\ \alpha & 0 \end{bmatrix}.$$

Consequently, the relationship between acceleration of points O and P expressed in matrix form is

$$\mathbf{a}_P = \mathbf{a}_O + \begin{bmatrix} -r_{1,P} & -r_{2,P} \\ -r_{2,P} & r_{1,P} \end{bmatrix} \begin{bmatrix} \omega^2 \\ \alpha \end{bmatrix}.$$

Equivalently,

$$\mathbf{a}_P = \mathbf{a}_O + D(\mathbf{r}_P)\mathbf{y}$$

where

$$D(\mathbf{r}) = \begin{bmatrix} -r_1 & -r_2 \\ -r_2 & r_1 \end{bmatrix}, \quad \mathbf{y} = \begin{bmatrix} \omega^2 \\ \alpha \end{bmatrix}.$$

APPENDIX II

DERIVATION FOR MATRICES \widehat{D} , E , G , AND F

The mean of true sensor acceleration $\bar{\mathbf{a}}$, placement $\bar{\mathbf{r}}$, measurement $\tilde{\mathbf{r}}$, and noise $\bar{\mathbf{e}}$ can be written as

$$\bar{\mathbf{v}} = F_m \mathbf{v}, \quad \text{where } \mathbf{v} = \{\mathbf{a}, \mathbf{r}, \mathbf{a}', \mathbf{e}\}.$$

Similarly, for the i th accelerometer, the relative quantity from the mean is defined using a tilde $\tilde{\mathbf{v}}_i$

$$\tilde{\mathbf{v}}_i = \mathbf{v}_i - \bar{\mathbf{v}}, \quad \text{where } \mathbf{v} = \{\mathbf{a}, \mathbf{r}, \mathbf{a}', \mathbf{e}\}.$$

Let \mathbf{a}_B denote the linear acceleration of the origin B of the coordinate system. From rigid body mechanics, we know that

$$\begin{aligned} \mathbf{a}_i &= \mathbf{a}_B + D(\mathbf{r}_i)\mathbf{y}, \quad \bar{\mathbf{a}} = \mathbf{a}_B + D(\bar{\mathbf{r}})\mathbf{y} \Rightarrow \tilde{\mathbf{a}}_i = D(\tilde{\mathbf{r}}_i)\mathbf{y} \\ \tilde{\mathbf{a}} &= \begin{bmatrix} \tilde{\mathbf{a}}_1 \\ \tilde{\mathbf{a}}_2 \\ \vdots \\ \tilde{\mathbf{a}}_{N_j} \end{bmatrix} = \underbrace{\begin{bmatrix} D(\tilde{\mathbf{r}}_1) \\ D(\tilde{\mathbf{r}}_2) \\ \vdots \\ D(\tilde{\mathbf{r}}_{N_j}) \end{bmatrix}}_{\widehat{D}} \mathbf{y} = \underbrace{\left(\mathbf{1}_{N_j} - \begin{bmatrix} F_m \\ \vdots \\ \times_{N_j} \end{bmatrix} \right)}_E \mathbf{a} \\ \Rightarrow \tilde{\mathbf{a}} &= \widehat{D}\mathbf{y} = E(\mathbf{a}' - \mathbf{e}) \\ \Rightarrow \mathbf{y} &= \underbrace{\widehat{D}^+ E}_{G}(\mathbf{a}' - \mathbf{e}). \end{aligned}$$

The acceleration of point O is

$$\tilde{\mathbf{a}}_O = D(\tilde{\mathbf{r}}_O)\mathbf{y} \Rightarrow \mathbf{a}_O = \underbrace{(F_m + D(\tilde{\mathbf{r}}_O)G)}_F(\mathbf{a}' - \mathbf{e}).$$

APPENDIX III

SIMULATION OF SLIDER CRANK MOTION

The slider crank motion is simulated in the following manner.

- Input:* a) Link lengths L_a , L_b and $\lambda = L_a/L_b$.
b) $\theta_a(t)$ as a continuously differentiable function, e.g., $\theta_a(t) = A \sin(2\pi ft)$.

Step 1: Calculate link a angular parameters

$$\omega_a = \frac{d\theta_a}{dt}, \quad \omega_a = \frac{d\omega_a}{dt}.$$

Step 2: Calculate link b angular parameters

$$\begin{aligned} \theta_b &= \sin^{-1}(-\lambda \sin \theta_a), \quad \omega_b = -\lambda \left(\frac{\cos \theta_a}{\cos \theta_b} \right) \omega_a \\ \alpha_b &= \lambda \left(\frac{\sin \theta_a (\omega_a^2 - \omega_b^2) - \cos \theta_a \alpha_a}{\cos \theta_b} \right). \end{aligned}$$

Step 3: Joint angle acceleration in the two link reference frames using (2) and $\theta_{ab} = \theta_a - \theta_b$

$$\begin{aligned} \mathbf{a}_O^a &= D \left(\begin{bmatrix} L_a \\ 0 \end{bmatrix} \right) \begin{bmatrix} \omega_a^2 \\ \alpha_a \end{bmatrix} \\ \mathbf{a}_O^b &= \begin{bmatrix} \cos(\theta_{ab}) & -\sin(\theta_{ab}) \\ \sin(\theta_{ab}) & \cos(\theta_{ab}) \end{bmatrix} \mathbf{a}_O^a. \end{aligned}$$

Step 4: Calculate true acceleration \mathbf{a}_i using (2) given the position of the accelerometers.

Step 5: Calculate noisy accelerometer readings \mathbf{a}'_i using (3).

APPENDIX IV ACCELEROMETER CALIBRATION USING LINEAR LEAST SQUARES

For a given sensor, the linear relationship between the acceleration \mathbf{a} and sensor signal \mathbf{v} is defined using sensitivity S and offset \mathbf{o}

$$\widehat{\mathbf{a}} = S\mathbf{v} + \mathbf{o}$$

for $S \in \mathbb{R}^{3 \times 3}$ and $\widehat{\mathbf{a}}, \mathbf{v}, \mathbf{o} \in \mathbb{R}^{3 \times 1}$. This is rewritten as

$$\widehat{\mathbf{a}} = V(\mathbf{v})\mathbf{y}$$

$$V(\mathbf{v}) = \begin{bmatrix} \mathbf{v}^T & 0 & 0 & 1 & 0 & 0 \\ 0 & \mathbf{v}^T & 0 & 0 & 1 & 0 \\ 0 & 0 & \mathbf{v}^T & 0 & 0 & 1 \end{bmatrix}$$

$$\mathbf{y} = [S_{11}, S_{12}, S_{13}, S_{21}, S_{22}, S_{23}, S_{31}, S_{32}, S_{33}, o_1, o_2, o_3]^T.$$

Accelerometer readings are taken from known orientations $\pm x$, $\pm y$, and $\pm z$ (calibration poses). It can be observed that only four linearly independent orientations are required for obtaining the unknowns. Consequently, the calibration constants, \mathbf{y} , are calculated using linear least squares solution

$$\mathbf{y} = \mathcal{V}^+ \mathcal{A}$$

$$\mathcal{A} = [\widehat{\mathbf{a}}_1^T, \widehat{\mathbf{a}}_2^T, \dots, \widehat{\mathbf{a}}_N^T]^T$$

$$\mathcal{V} = [V(\mathbf{v}_1)^T, V(\mathbf{v}_2)^T, \dots, V(\mathbf{v}_N)^T]^T$$

where $\mathcal{A} \in \mathbb{R}^{3N \times 1}$, $\mathcal{V} \in \mathbb{R}^{3N \times 12}$, and the superscript $+$ denotes the pseudoinverse of the matrix.

REFERENCES

- [1] V. Bonnet, V. Joukov, D. Kulić, P. Fraisse, N. Ramdani, and G. Venture, "Monitoring of hip and knee joint angles using a single inertial measurement unit during lower limb rehabilitation," *IEEE Sensors J.*, vol. 16, no. 6, pp. 1557–1564, Mar. 2016.
- [2] F. Ghassemi, S. Tafazoli, P. D. Lawrence, and K. Hashtrudi-Zaad, "Design and calibration of an integration-free accelerometer-based joint-angle sensor," *IEEE Trans. Instrum. Meas.*, vol. 57, no. 1, pp. 150–159, Jan. 2008.
- [3] J. Viñonen, J. Mattila, and A. Visa, "Joint-space kinematic model for gravity-referenced joint angle estimation of heavy-duty manipulators," *IEEE Trans. Instrum. Meas.*, vol. 66, no. 12, pp. 3280–3288, Dec. 2017.
- [4] C. N. Teague *et al.*, "A wearable, multimodal sensing system to monitor knee joint health," *IEEE Sensors J.*, vol. 20, no. 18, pp. 10323–10334, Sep. 2020.
- [5] R. Williamson and B. J. Andrews, "Detecting absolute human knee angle and angular velocity using accelerometers and rate gyroscopes," *Med. Biol. Eng. Comput.*, vol. 39, no. 3, pp. 294–302, May 2001.
- [6] M. El-Gohary and J. McNames, "Human joint angle estimation with inertial sensors and validation with a robot arm," *IEEE Trans. Biomed. Eng.*, vol. 62, no. 7, pp. 1759–1767, Jul. 2015.
- [7] M. El-Gohary and J. McNames, "Shoulder and elbow joint angle tracking with inertial sensors," *IEEE Trans. Biomed. Eng.*, vol. 59, no. 9, pp. 2635–2641, Jun. 2012.
- [8] A. Tognetti, F. Lorusso, N. Carbonaro, and D. de Rossi, "Wearable goniometer and accelerometer sensory fusion for knee joint angle measurement in daily life," *Sensors*, vol. 15, no. 11, pp. 28435–28455, Nov. 2015.
- [9] S. Majumder and M. J. Deen, "Wearable IMU-based system for real-time monitoring of lower-limb joints," *IEEE Sensors J.*, vol. 21, no. 6, pp. 8267–8275, Dec. 2021.
- [10] F. Olsson, M. Kok, T. Seel, and K. Halvorsen, "Validity and reliability of wearable sensors for joint angle estimation: A systematic review," *Sensors*, vol. 20, no. 12, p. 1555, 2020.
- [11] S. Majumder and M. J. Deen, "A robust orientation filter for wearable sensing applications," *IEEE Sensors J.*, vol. 20, no. 23, pp. 14228–14236, Dec. 2020.
- [12] Y. Mengue *et al.*, "Soft wearable motion sensing suit for lower limb biomechanics measurements," in *Proc. IEEE Int. Conf. Robot. Autom.*, May 2013, pp. 5309–5316.
- [13] A. H. Zorn, "A merging of system technologies: All-accelerometer inertial navigation and gravity gradiometry," in *Proc. IEEE Position Location Navigat. Symp.*, Apr. 2002, pp. 66–73.
- [14] T. Seel, J. Raisch, and T. Schauer, "IMU-based joint angle measurement for gait analysis," *Sensors*, vol. 14, no. 4, pp. 6891–6909, Jan. 2014.
- [15] A. P. L. Bo, M. Hayashibe, and P. Poignet, "Joint angle estimation in rehabilitation with inertial sensors and its integration with Kinect," in *Proc. Annu. Int. Conf. IEEE Eng. Med. Biol. Soc.*, Aug. 2011, pp. 3479–3483.
- [16] I. Weygers *et al.*, "Drift-free inertial sensor-based joint kinematics for long-term arbitrary movements," *IEEE Sensors J.*, vol. 20, no. 14, pp. 7969–7979, Mar. 2020.
- [17] G. Cooper *et al.*, "Inertial sensor-based knee flexion/extension angle estimation," *J. Biomech.*, vol. 42, no. 16, pp. 2678–2685, 2009.
- [18] F. Olsson, M. Kok, T. Seel, and K. Halvorsen, "Robust plug-and-play joint axis estimation using inertial sensors," *Sensors*, vol. 20, no. 12, p. 3534, Jun. 2020.
- [19] P. Cheng and B. Oelmann, "Joint-angle measurement using accelerometers and gyroscopes—A survey," *IEEE Trans. Instrum. Meas.*, vol. 59, no. 2, pp. 404–414, Feb. 2010.
- [20] V. Vikas and C. D. Crane, III, "Joint angle measurement using strategically placed accelerometers and gyroscope," *ASME J. Mech. Robot.*, vol. 8, no. 2, Nov. 2015, Art. no. 021003.
- [21] M. Maynard and V. Vikas, "Angular velocity estimation using non-coplanar accelerometer array," *IEEE Sensors J.*, vol. 21, no. 20, pp. 23452–23459, Oct. 2021.
- [22] G. Welch *et al.*, "An introduction to the Kalman filter," Univ. North Carolina Chapel Hill, Chapel Hill, NC, USA, Tech. Rep. TR 95-041, 1995. [Online]. Available: <https://citeseerx.ist.psu.edu/viewdoc/versions?doi=10.1.1.117.6808>
- [23] S. J. Julier and J. K. Uhlmann, "Unscented filtering and nonlinear estimation," *Proc. IEEE*, vol. 92, no. 3, pp. 401–422, Mar. 2004.
- [24] E. A. Wan and R. Van Der Merwe, "The unscented Kalman filter for nonlinear estimation," in *Proc. IEEE Adapt. Syst. Signal Process., Commun., Control Symp.*, Oct. 2000, pp. 153–158.
- [25] J. H. Ginsberg, *Advanced Engineering Dynamics*. Cambridge, U.K.: Cambridge Univ. Press, 1998.



Cole Woods (Student Member, IEEE) was born in Fairhope, AL, USA. He received the B.S. degree in mechanical engineering and the master's degree in business administration from the University of Alabama, Tuscaloosa, AL, USA, in 2019 and 2020, respectively, where he is currently pursuing the Ph.D. degree in mechanical engineering with the Agile Robotics Lab (ARL).

His research interests include inertial sensing and tensegrity mechanisms.



Vishesh Vikas (Member, IEEE) was born in New Delhi, India. He received the B.Tech. degree from the Indian Institute of Technology Guwahati, Guwahati, India, in 2005, and the Ph.D. degree in mechanical engineering from the University of Florida, Gainesville, FL, USA, in 2011.

Since 2016, he has been an Assistant Professor of Mechanical Engineering with the University of Alabama, Tuscaloosa, AL, USA, where he directs the Agile Robotics Lab. His research interests include soft robotics, tensegrity robotics, agriculture robotics, and optimal estimation.